Article

# Effect of Sn on the CO Catalytic Activity and Water Resistance of Cu−Mn Catalyst

Yashengnan Sun,* Xihua Zhou, Tianyu Xin, Gang Bai, Yumeng Wang, Xianlin Li, and Xiao Mufeng

Read Online

ACCESS | Metrics & More | Article Recommendations

**ABSTRACT:** In view of the problem that excessive CO in underground coal mine space can easily lead to a large number of casualties, Cu−Mn−Sn water-resistant eliminators with different Sn contents were prepared by a co-precipitation method. The activity of the eliminators was analyzed by using an independently developed activity testing platform, $N_2$ adsorption and desorption, XRD, SEM, XPS, and FTIR to characterize the activity factors and water resistance. The results showed that Cu−Mn−Sn-20 with 20% Sn content had the highest activity, which was 3.23 times that of Cu−Mn. The main reason for the increased activity is that Cu−Mn−Sn-20 doped with 20% Sn provides a larger specific surface area and more active sites and reduces the pore size, so that the crystallization degree of $Cu_{1.4}Mn_{1.5}O_4$ is lower. The doping of 20% Sn reduces the absorption of lattice water and coordination water and improves the water resistance of Cu−Mn−Sn-type eliminators. The Cu−Mn−Sn-20 water-resistant eliminator is used to quickly eliminate CO in underground coal mines, which is of great significance for the rescue workers in underground coal mines after disasters.
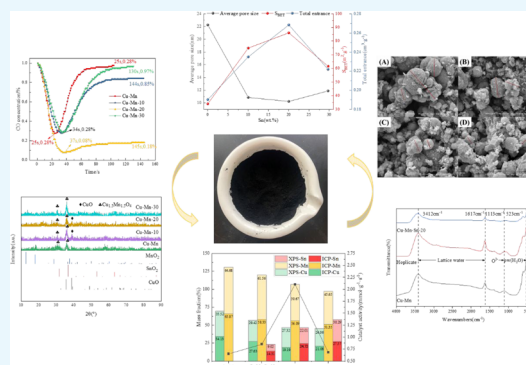
## 1. INTRODUCTION

Underground coal mines are usually poorly ventilated.[1] Consequently, toxic and harmful gases may accumulate in these relatively closed spaces. This phenomenon remarkably reduces the air quality in the coal mine. Accumulation of coal mine gas and coal dust explosion,[2,3] coal fire,[4,5] and blasting operations in mines[6,7] unavoidably produce huge amounts of carbon monoxide (CO) in the mine atmosphere. When a large amount of CO gas is inhaled by a person, it easily combines with hemoglobin in the blood, which results in hypoxia, suffocation, and even death.[8,9] Accordingly, it is essential to remove CO from the coal mine atmosphere.

Underground coal mines usually have a harsh environment,[10,11] and the humidity of some areas may exceed 95%.[12−14] Currently, Cu−Mn is the most widely used catalyst to remove CO from environments with a humidity of higher than 45%.[15,16] In order to improve the CO removal efficiency of the catalyst in the underground coal mine and reduce the adverse impact of water vapor on the removal performance of the catalyst, it is necessary to improve the water resistance of the eliminator.

In this regard, Bae et al.[17] doped lanthanum (La) on the surface of $Co_3O_4$ and found that La doping prevents the adsorption and desorption of $H_2O$, thereby reducing the formation of −OH groups on the catalyst surface and improving the water-resistance of $Co_3O_4$ components. Yang et al.[18] synthesized Co-doped manganese octahedral molecular sieves with an ordered cryptomelane structure (OMS-2) via a

one-step hydrothermal method and improved the surface hydrophobicity of the catalyst. Moreover, Li et al.[19] prepared a series of Pt/Fe-coloaded mBeta using an ion-exchange process and the ethylene glycol reduction method and achieved high water resistance. Yin et al.[20] developed an innovative oxygen vacancy-rich nitrogen-doped $Co_3O_4$ catalyst using the straightforward urea-assisted method. Comparing the performance of pure $Co_3O_4$ and $Co_3O_4$ with less nitrogen doping revealed that the as-synthesized nitrogen-doped $Co_3O_4$ has significantly higher performance and water resistance in the catalytic oxidation of CO. On the basis of the solid-phase method, Zhou et al.[21] developed a series of $M_3Co_{16}O_x$ (M = Cr, Ti, Zr, Fe, Mn) oxide catalysts wrapped by the polymer nanofilm. At low vapor levels (e.g., 3.1 vol %) and low temperatures (e.g., 85 °C), $M_3Co_{16}O_x$ has long-term catalytic stability (>1 month). Shen et al.[22] synthesized polymer nanofilm-coated $Fe_aCo_bO_x$ catalysts using a solid-phase method mediated with oxalic acid (OA)/ethylene glycol (EG) for low-temperature CO oxidation. Further investigations show that even when the medium is subjected to low

humidity (e.g., 3.1 vol %) and a low temperature (e.g., 90 °C) for more than 1 month, the adverse impact on the activity is small. Zhang et al.[23] synthesized a highly active Ag/Fe$_2$O$_3$ catalyst using the impregnation method. It was found that among the studied cases, the highest activity, stability, and resistance to water vapor and the largest specific surface area can be achieved in Ag/Fe$_2$O$_3$ catalyst with a Fe/Ag atomic ratio of 15.

Although the above-mentioned methods have remarkably improved the water-resistance index of catalysts, they often have a complicated preparation and are not applicable in most raw materials. Liu et al. found that tin (Sn) doping can improve the resistance to water of the catalyst.[16,24−26] Considering the low cost of raw materials and simplicity of the preparation method, a series of Cu−Mn−Sn catalysts with different Sn contents have been prepared using the co-precipitation method. The Cu−Mn−Sn catalyst was characterized by N$_2$ adsorption and desorption, XRD, XPS, FTIR, and activity testing techniques to analyze the effects of Sn content on the pore structure, surface morphology, phase change, catalytic activity, and resistance to water of the catalyst. Accordingly, the optimum ratio of catalyst is selected to improve the adaptability of CO catalyst in underground coal mines.

## 2. EXPERIMENTAL SECTION

**2.1. Raw Materials.** Experimental reagents needed in the preparation of eliminator are shown in Table 1.

**Table 1. Experimental Reagent**

| reagent | molecular weight | purity | source |
|---|---|---|---|
| Cu(NO$_3$)$_2$·3H$_2$O | 179.544 | ≥99% | Sinopharm Chemical Reagent Co. Ltd. |
| Mn(NO$_3$)$_2$ | 178.946 | 50 wt % | Sinopharm Chemical Reagent Co. Ltd. |
| SnCl$_4$·5H$_2$O | 350.412 | ≥99% | Sinopharm Chemical Reagent Co. Ltd. |
| Na$_2$CO$_3$ | 105.986 | ≥99% | Sinopharm Chemical Reagent Co. Ltd. |

**2.2. Preparation of Catalysts.** Cai et al.[27] synthesized Cu−Mn oxide with different precursors and sediments using a co-precipitation method as the CO eliminator. Li et al.[3,4] prepared Cu−Mn catalyst samples using a hydrothermal method as the CO eliminatorn. Therefore, when only Cu and Mn elements are contained in the eliminator, the ratio of Cu to Mn mass fraction is controlled at 1:2 in the preparation of the eliminator, and the CO elimination performance is higher.

Since Sn does not participate in the catalytic oxidation reaction,[16] the Cu−Mn type remover has the highest removal performance when the mass fraction ratio of Cu/Mn is 1:2. When Cu−Mn−Sn was prepared as the eliminator, the mass fraction ratio of Cu to Mn was controlled at 1:2. The Sn contents were 0% (Cu−Mn), 10% (Cu−Mn−Sn-10), 20% (Cu−Mn−Sn-20), and 30% (Cu−Mn−Sn-30).

Cu(NO$_3$)$_2$·3H$_2$O(aq, 0.58 mol·L$^{-1}$), Mn(NO$_3$)$_2$(aq, 50 wt %), and SnCl$_4$·5H$_2$O(aq, 0.16 mol·L$^{-1}$) were mixed uniformly in proportion. Na$_2$CO$_3$(aq, 2.5 mol·L$^{-1}$) was dropped into a three-mouth flask, and the water bath magnetic stirring device (purchased from Nanguan Mecot Laboratory Instrument Agency, model DF-101S, heating temperature: rt to 400 °C) kept the temperature of Na$_2$CO$_3$ aqueous solution stable at 70 °C under vigorous stirring. Dilute nitric acid (aq, 2 mol·L$^{-1}$) was dropped into the above solution mixture, a pH meter was used (purchased from Nanguan District Mecot Experimental Instrument Agency, model PHS-3C pH: 0.00−14.00) to test the pH of the solution until the pH reached 8.3, and then a water bath magnetic stirring device was used to continue the stirring for 4 h at a constant temperature of 70 °C. Finally, a circulating water multipurpose vacuum pump (purchased from Nanguan district Mecot Experimental Instrument Agency, model SHB-D (III)) was used to wash the sediment. An electric air-blowing drying oven (purchased from Wuhan Yahua Electric Furnace Co., Ltd., model 101-1AB, drying temperature: rt to 1000 °C) was used for drying, a muffle furnace (purchased from Wuhan Yahua Electric Furnace Co., Ltd., model YHA-5000, calcination temperature: rt to 1000 °C, heating rate: 0−10 °C/min) was used for calcination, and after
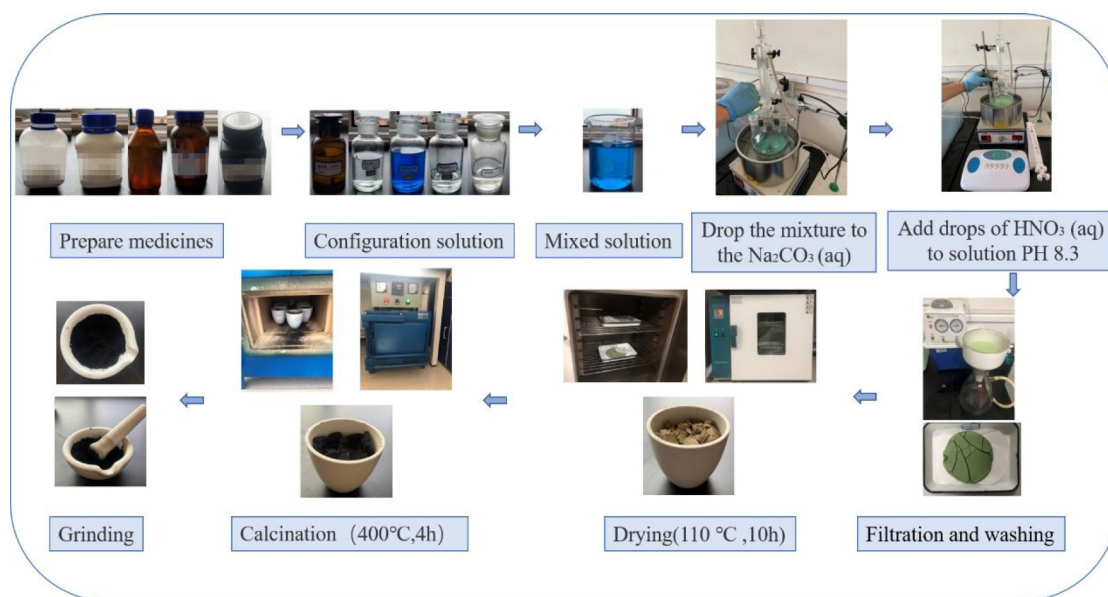


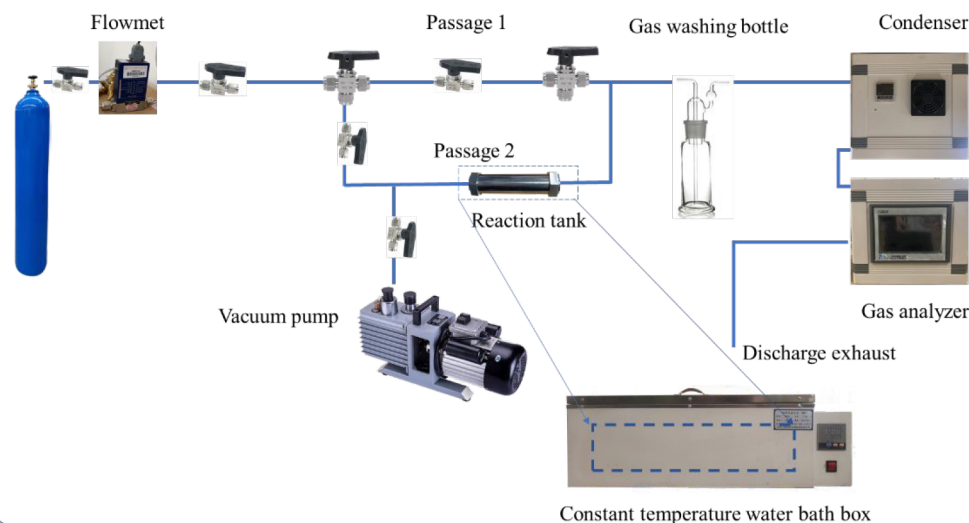**Figure 1.** Elimination agent preparation process.

**Figure 2.** Activity test experimental system.

grinding, the preparation of the eliminating agent was complete. The preparation flowchart is shown in Figure 1.

**2.3. Characterization Techniques.** The specific surface area and pore size of the eliminator have a great influence on the activity of the eliminator. The BET method and BJH method were used to calculate the specific surface area and the pore size of the eliminator for $N_2$ adsorption−desorption measurements at 77 K.

In order to compare the surface microstructure of Cu−Mn−Sn with different Sn contents, the eliminator was characterized by SEM. Scanning electron microscope (SEM) images were taken on a ZEISS MERLIN Compac scanning electron microscope.

In order to accurately determine the element content of the sample, the samples were analyzed by ICP-OES using an Agilent 720 spectrometer.

To determine the composition of eliminators with different Sn contents, an X-ray diffractometer (Rigaku Ultima IV X-ray diffractometer) was used to analyze the phase of eliminators with different Sn contents. First, the sample was screened to 250 meshes, and the powder was loaded onto a special experimental slide ready for scanning. Experimental conditions: copper target value is 1.5416A, tube voltage and tube current are 45 kV and 40 mA, respectively. The diffraction slit is 1°, the receiving slit is 0.1 mm, and the scanning mode is continuous. The scanning range is 10−90°, the speed is 5°/min, and the sampling interval is 0.02°. MDI Jade 6.5 software was used to analyze the diffraction pattern, and the phase analysis of the sample was obtained.

In order to obtain the metal composition on the surface of the eliminant, X-ray photoelectron spectroscopy was used to scan the full spectrum and fine spectrum of the elements on the surface, and Avantage software was used to process the spectrum. Experimental conditions: X-ray excitation source is Al Kα ray (0.6 eV), beam spot is 400 $\mu$m, vacuum degree of analysis room is ∼3 × 10$^{-7}$ MBA, working voltage is 12 kV, filament current is 6 mA, full spectrum scanning is 150 eV, step length is 1 eV, narrow spectrum scanning is 50 eV, and the step length is 0.1 eV. Surface contamination C 1s (284.8 eV) was used as the standard for correction.

**2.4. Catalyst Activity Test.** The eliminator is based on the principle of chemical catalysis. In a catalytic reaction, the level

of activity indicates the strength of the elimination agent to accelerate the reaction. Thus, the activity of the eliminator is defined as the rate of catalytic reaction. The activity per unit mass of eliminator was used as the optimum index. The reaction rate is defined as formula 1.

$$\dot{\xi} \overset{\text{def}}{=} \frac{d\xi}{dt} \tag{1}$$

$\xi$ is the reaction degree and is defined as formula 2.

$$d\xi \overset{\text{def}}{=} \frac{\Delta n_{B_i}}{v_i} \tag{2}$$

$\Delta n_{B_i}$ is the variation of component $B_i$ (mol).

The ideal gas state equation is shown in formula 3.

$$pV = nRT \tag{3}$$

$p$ is pressure (Pa), $V$ is the volume of the gas (m$^3$), $T$ is temperature (K), $n$ is the moles of the gas (mol), and $R$ is the molar gas constant, 8.314472 J·mol$^{-1}$·K$^{-1}$.

The amount of substance in which CO changes is shown in formula 4.

$$\Delta n_{B_i} = n_{B_i} - n_{B_i}^0 = \frac{P}{RT} \int_0^t V_{B_i} \, dt \tag{4}$$

The volume change of CO is calculated as shown in formula 5.

$$V_{B_i} = \frac{L}{60}(c - c_0)t \times 10^{-6} \tag{5}$$

The activity calculation is shown in formula 6.

$$s = \frac{1}{m} \cdot \frac{d\xi}{dt} \tag{6}$$

$n_{B_i}$ and $n_{B_i}^0$ are the amount of substance $i$ at time $t$ and time $t = 0$ (mol). $v_i$ is the stoichiometric coefficient of CO. $m$ is the mass of catalyst (g). $s$ is the activity of the eliminator (mol·g$^{-1}$·s$^{-1}$). $V_{B_i}$ is the instantaneous volume change of CO during ablation (m$^3$). $L$ is the mixed gas flow rate (mL/min). $t$ is the reaction equilibrium time (s). $c$ is the instantaneous concentration of CO tested (%). $c_0$ is the initial concentration of CO in the mixed gas (%).

The dynamic method was used to test the activity of the eliminator and analyze its eliminator performance. The experimental system diagram of activity test is shown in Figure 2.

Experimental steps:

*1. Air Tightness Inspection of the Experimental System.* In order to ensure the accuracy and reliability of the experimental results, it is necessary to check the air tightness of the experimental system before the experiment. Under the condition that there is no sample in the reaction tank, 0.2 MPa $N_2$ was fed into the experimental system, all valves of the experimental system were closed, and all pipeline connections and the interface of the reaction tank with leak detection fluid were checked. No bubbles were generated, indicating good air tightness.

*2. Experimental System Detection.* The reaction tank that was not put in the eliminator was put under vacuum and filled with 0.12 MPa standard gas. The temperature of the tank was controlled at 25 °C. No change in the concentration of each gas was observed under experimental conditions. Therefore, the reactivity of the tank materials and the spontaneous reaction of CO and $O_2$ can be ignored under the experimental conditions.

*3. Vacuum.* A vacuum pump was used to vacuum the experimental system.

*4. Placement of the Sample.* Use an electronic balance to weigh the sample (10 g), the eliminant sample was placed in the reaction tank, and 3 cm filter cotton was placed in the front and back of the reaction tank to ensure the sample was fixed and to prevent dust pollution of the gas analyzer in the process of gas flow.

*5. Constant Temperature.* The temperature of the water bath chamber was set to 25 °C, and the experiment was conducted after it was stable for 2h.

*6. Flow Adjustment.* The flow rate was adjusted to 80 mL/ min using a flowmeter.

*7. Stable Gas Analyzer Number.* The cylinder valve was opened and the mixed gas was allowed to pass through passage 1, waiting until the amount of CO, $O_2$, and $CO_2$ on the gas analyzer was stable.

*8. Test.* The three-way valve was used to make the gas pass through passage 2, and the concentration changes of CO, $O_2$, and $CO_2$ gas were recorded and analyzed.

## 3. RESULTS AND DISCUSSION

**3.1. Catalyst Activity.** In order to analyze the activity of each sample in the process of CO removal, the instantaneous CO reaction amount after the mixed gas was injected into the reaction tank was calculated according to Formula 4. The variation curve of CO concentration of each sample in the process of CO removal over time is shown in Figure 3. As can be seen from Figure 3, the change curve of CO concentration of each sample over time first increased and then decreased. When the mixed gas starts to pass through the eliminator, the active sites on the eliminator surface are not fully occupied, and the CO molecule rapidly combines with the active sites on the eliminator surface when passing through, resulting in the rapid decline of the CO concentration curve. With the binding of CO molecule to the active site, the active site on the surface of the eliminator gradually decreased, and the elimination ability of CO molecule gradually weakened until the equilibrium was reached.
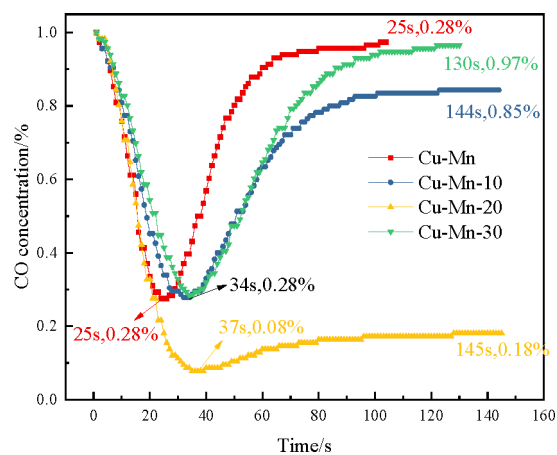


**Figure 3.** CO concentration of each sample in the elimination process varies with time in dry environment.

It can be seen from Figure 3 that there are two inflection points in the change curve of CO concentration, namely, the lowest concentration point and the equilibrium point, as shown in Figure 4. When the Sn content is 20%, the lowest
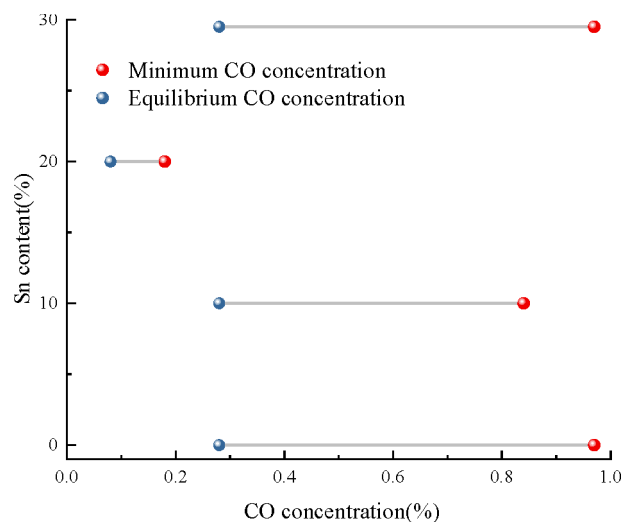


**Figure 4.** Influence of Sn content on the inflection point of the ablation process.

instantaneous concentration of CO is the lowest, and the equilibrium concentration is also in the lowest state when the elimination equilibrium, so its activity is also the highest. In CO elimination equilibrium, the equilibrium concentrations of Cu−Mn, Cu−Mn−Sn-10, and Cu−Mn−Sn-30 samples with Sn content of 0%, 10%, and 30% are close to the standard gas concentration of 1%, indicating that their stability is poor and elimination ability is weak. The CO equilibrium concentration of the Cu−Mn−Sn-20 sample with 20% Sn content is 0.18%, and the Cu−Mn−Sn-20 equilibrium concentration is the lowest.

The activity curve of eliminator varied with Sn content as shown in Figure 5. The activity of Cu−Mn, Cu−Mn-Sn-10, Cu−Mn−Sn-20, and Cu−Mn−Sn-30 were $0.65 \times 10^{-33}$ mmol $g^{-1}$ $s^{-1}$, $0.85 \times 10^{-3}$ mmol $g^{-1}$ $s^{-1}$, $2.10 \times 10^{-3}$ mmol $g^{-1}$ $s^{-1}$, and $0.68 \times 10^{-3}$ mmol $g^{-1}$ $s^{-1}$, respectively. The activity of Cu−Mn−Sn-20 with 20% Sn content was the highest. The
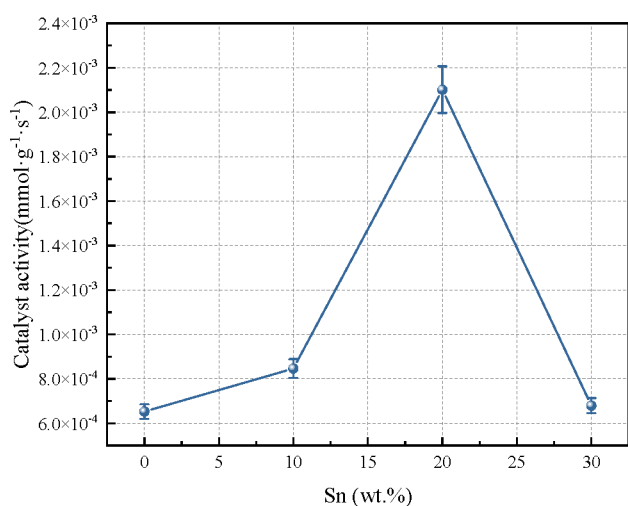
**Figure 5.** Activity of ablative agent varies with the content of Sn.

mesoporous. The hysteresis loops of samples with different Sn contents were H3-type hysteresis loops, and the mesoporous shape was a slit shaped by particle accumulation. As the main pore sizes of Cu−Mn, Cu−Mn−Sn-10, Cu−Mn−Sn-20, and Cu−Mn−Sn-30 samples were mesoporous, the BJH method was used to calculate the pore size distribution of the samples, as shown in Figure 6.

The specific surface area of each sample eliminator calculated according to the BET equation is shown in Figure 7. As can be seen from Figure 7, the specific surface area of the
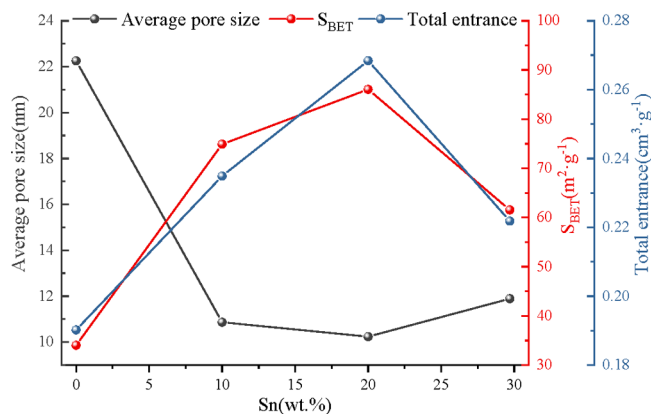


**Figure 7.** Specific surface area, average pore size, and total entrance of samples with different Sn contents.

reasons for the increased activity of Cu−Mn−Sn-20 were analyzed by subsequent experiments.

**3.2. Catalyst Pore Characteristics.** $N_2$ adsorption and desorption were used to measure the isothermal adsorption curve and pore size distribution of the eliminator, as shown in Figure 6.

As can be seen from Figure 6, when the relative pressure of each sample is 0.4 MPa, the adsorbent capillary gathers, and the isotherm rises at a fast rate. Sample attachment curves are located above the adsorption curve, resulting in adsorption hysteresis, which conforms to the characteristics of the type IV isotherm. The pore structure of each sample is mainly

prepared remover with different Sn contents presents an inverted U-shaped curve with increasing Sn content. The specific surface area first increases and then decreases with the increase of Sn content. The maximum specific surface area
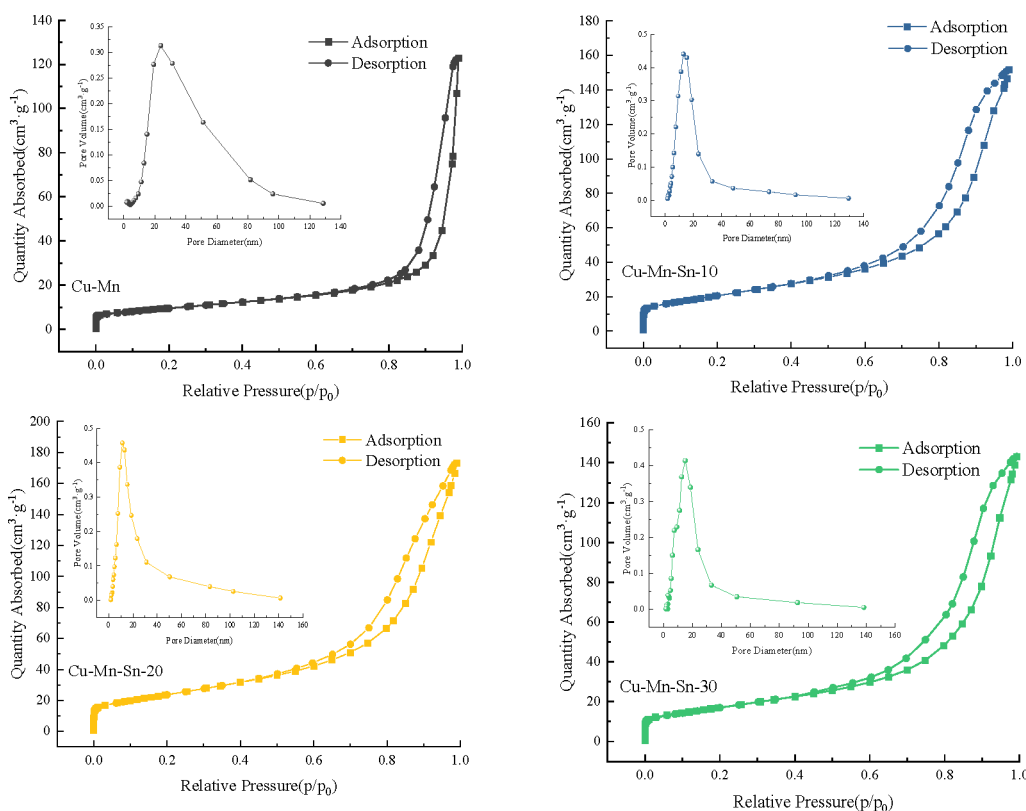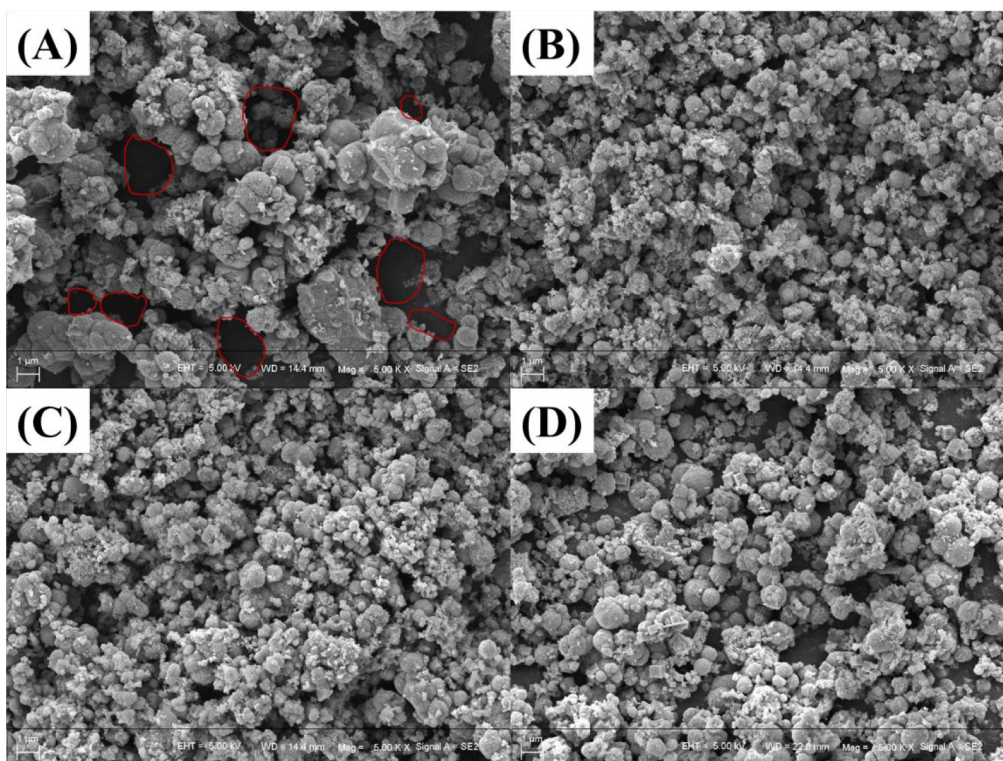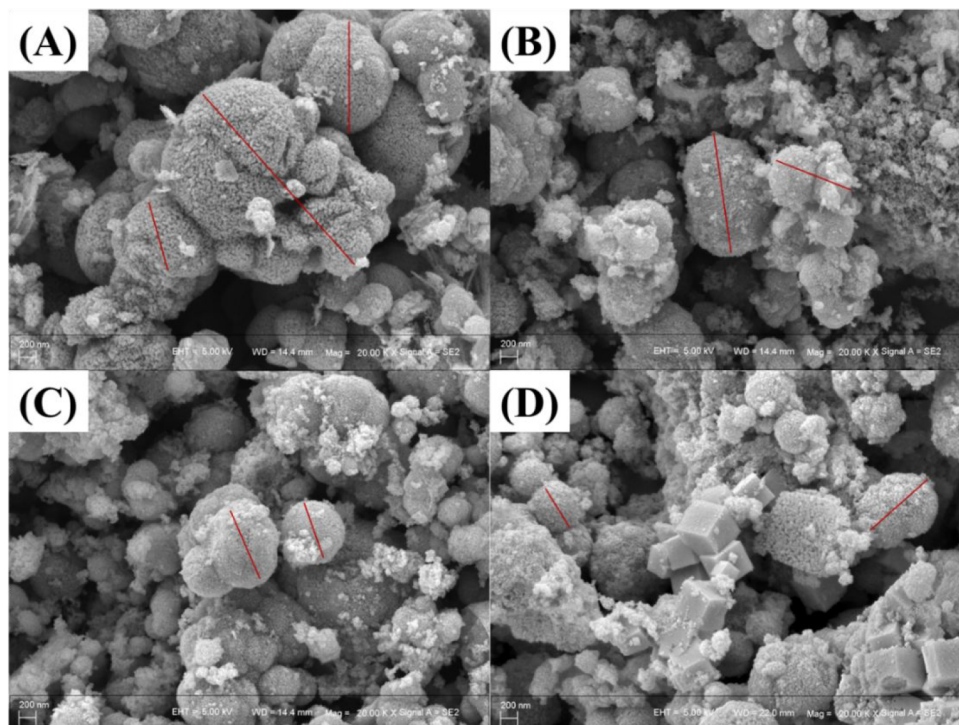


**Figure 6.** Adsorption isotherms and pore diameter profiles of ablators with different Sn contents.

**Figure 8.** SEM micrographss of Cu−Mn−Sn composite oxides with different Sn contents. (A) Cu−Mn, (B) Cu−Mn−Sn-10, (C) Cu−Mn−Sn-20, (D) Cu−Mn−Sn-30.



**Figure 9.** SEM micrographss of Cu−Mn−Sn composite oxides with different Sn contents. (A) Cu−Mn, (B) Cu−Mn−Sn-10, (C) Cu−Mn−Sn-20, (D) Cu−Mn−Sn-30.

appears when the Sn content is 20%, and the specific surface area increases by 153% compared with the sample with 0% Sn content. The addition of Sn is helpful to increase the specific surface orea of the Cu−Mn sample, which is also the reason for its increased activity.

As can be seen from the pore size distribution curve in Figure 6, the pore size distribution of Cu−Mn is relatively dispersed, and the pore size distribution of other samples is similar. Compared with Cu−Mn, the addition of Sn is helpful to improve the concentration of the pore size distribution. For

all samples, only one size of mesopores exists, and the average pore size and total pore volume of mesopores are shown in Figure 7. With the increase of Sn content, the difference of average pore size of each sample is small, and the change of total pore volume reaches 0.27 cm$^3 \cdot$g$^{-1}$ at Cu−Mn−Sn-20 and then decreases. It indicates that Sn doping reduces the pore size of the eliminator and increases the total pore volume. When Sn content is 20%, the pore size of Cu−Mn−Sn-20 is 10.88 nm, which is closer to the molecular diameter of CO which is 0.376 nm, and improves the activity of the eliminator.

SEM was used to analyze the pores of each sample of the eliminant. The SEM images of Cu−Mn−Sn composite oxides with different Sn contents are shown in Figure 8, and the scale is 1 μm. Figure 8 shows that a large number of intergranular mesoporous pores are formed in all samples, and Cu−Mn pores are significantly larger than those of Cu−Mn−Sn-10, Cu−Mn−Sn-20, and Cu−Mn−Sn-30 doped with Sn. The mesoporous sizes of Cu−Mn−Sn-10, Cu−Mn−Sn-20, and Cu−Mn−Sn-30 samples doped with Sn have small differences, which is consistent with the results of N$_2$ adsorption and desorption experiments.

**3.3. Surface Microstructure of Catalyst.** SEM was used to analyze the surface morphology of the eliminating agent. The SEM images of Cu−Mn−Sn composite oxides with different Sn contents are shown in Figure 9, and the scale is 200 nm.

It can be seen from Figure 9 that Cu−Mn, Cu−Mn−Sn-10, and Cu−Mn−Sn-20 have roughly the same morphology, showing round particles with irregular "villi" attached to spherical particles, while Cu−Mn−Sn-30 has obvious changes in morphology. In addition to round particles and "villi", cubes also appear. Some kind of Sn oxide may be formed due to the high Sn content. With Sn doping, the particles are significantly reduced and the stack pores are larger, which is the reason why Sn-doped samples have a larger specific surface area. Obviously, in the samples doped with Sn, Cu−Mn−Sn-20 particles are more uniform in size, more regular in shape, and have abundant mesoporous structures, providing larger specific surface area and more active sites. The Sn content has a significant effect on the surface morphology of the eliminator.

**3.4. Catalyst Composition.** As shown in Figure 10, compared with the peak values of standard cards CuO, MnO$_2$, and SnO$_2$, both Sn-doped and undoped composite metal oxide eliminators show low-intensity diffraction peaks, indicating that the heat resistance of the eliminators is significantly improved after calcination at 400 °C after a single metal oxide combination.

For all of the eliminant samples, the diffraction peak was observed to be more disorderly, and all of the samples had a low degree of crystallization. A low-intensity Cu$_{1.5}$Mn$_{1.5}$O$_4$ phase was observed in all samples, but no MnOx and SnOx phase was observed. It is believed that a large number of MnOx and SnOx phases exist in the elimination agent as an amorphous phase. The CuO phase was observed in Cu−Mn−Sn-10 and Cu−Mn−Sn-20. Obviously, the crystallization degree of the CuO phase in Cu−Mn−Sn-20 sample is higher, which may be the reason for the higher activity of the Cu−Mn−Sn-20 sample.

Cu−Mn, Cu−Mn−Sn-10, Cu−Mn−Sn-20, and Cu−Mn−Sn-30 all have the Cu$_{1.5}$Mn$_{1.5}$O$_4$ phase in their XRD curves, and the phase with the highest crystallization degree is the Cu$_{1.5}$Mn$_{1.5}$O$_4$ phase. It can be seen that the metal oxide with the highest content in each sample is Cu$_{1.5}$Mn$_{1.5}$O$_4$, which is
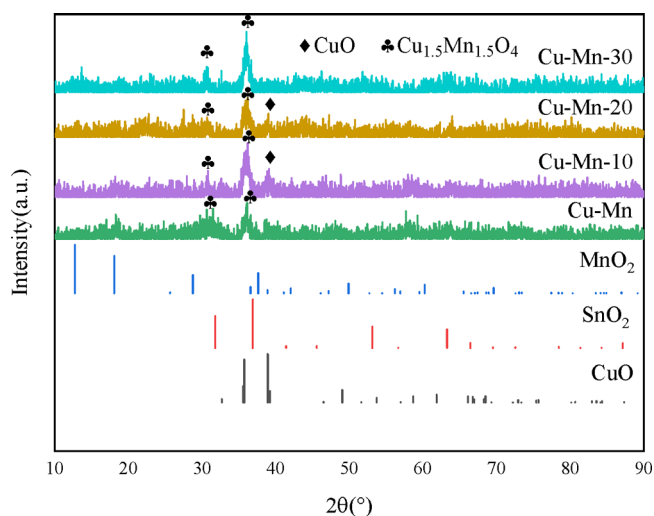


**Figure 10.** XRD patterns of Cu−Mn−Sn composite oxides with different Sn contents.

the main component of the eliminant. The Cu−Mn−Sn-20 sample Cu$_{1.5}$Mn$_{1.5}$O$_4$ phase crystallization degree is relatively low and its diffraction peak intensity is also low, but the sample activity is strong, indicating that the existence of Cu$_{1.5}$Mn$_{1.5}$O$_4$ phase is not conducive to improve the activity of the eliminator. The crystallization degree and diffraction peak intensity of the Cu$_{1.5}$Mn$_{1.5}$O$_4$ phase in the Cu−Mn−Sn-30 sample are obviously improved, indicating that excessive doping of Sn is beneficial to the formation of the Cu$_{1.5}$Mn$_{1.5}$O$_4$ phase but is not conducive to improving the activity of the elimination agent.

In order to understand the surface composition and element valence states of different Sn content eliminators, the full spectrum scanning of Cu−Mn, Cu−Mn−Sn-10, Cu−Mn−Sn-20, and Cu−Mn−Sn-30 was carried out by XPS technology, and the C 1s element with a binding energy of 284.8 eV was calibrated. The full spectrum and fineness of the calibrated data are shown in Figures 10 and 11.

According to the binding energy in Figure 11, the existence forms of Cu, Mn, Sn, and O elements are, respectively, Cu 2p, Mn 2p, Sn 3d, and O 1s, and fine spectral analysis is conducted for them as shown in Figure 12.

As can be seen from Figure 12, the binding energy of Sn and Cu is typical of Sn$^{4+}$ and Cu$^{2+}$,[26] indicating that they exist in the eliminator in a completely oxidized state. However, the binding energy of Mn indicates the existence of a mixed valence state in which Mn$_4^+$ dominates,[28] and a small amount of Mn$^{2+}$ and Mn$^{3+}$ may also exist in the eliminator. Cu−Mn, Cu−Mn−Sn-10, Cu−Mn−Sn-20, and Cu−Mn−Sn-30 samples all show shock peaks of about 940−945 eV, which are typical of Cu$^{2+}$, proving that Cu is completely oxidized in the solid solution sample.[29]

In order to explore the relationship between the surface element content and activity of Cu−Mn−Sn-10, Cu−Mn−Sn-20, and Cu−Mn−Sn-30, ICP-OES and XPS were used to test the surface content of Cn, Mn, and Sn elements on the surface of the eliminator and compare them with the activity, as shown in Figure 13.

Figure 13 shows the relationship between the content of Cn, Mn, and Sn on the surface of the eliminator and its activity. For CO oxidation on the eliminator, CO molecules are usually adsorbed on the Cu$^{2+}$ site first and activated first. Then it
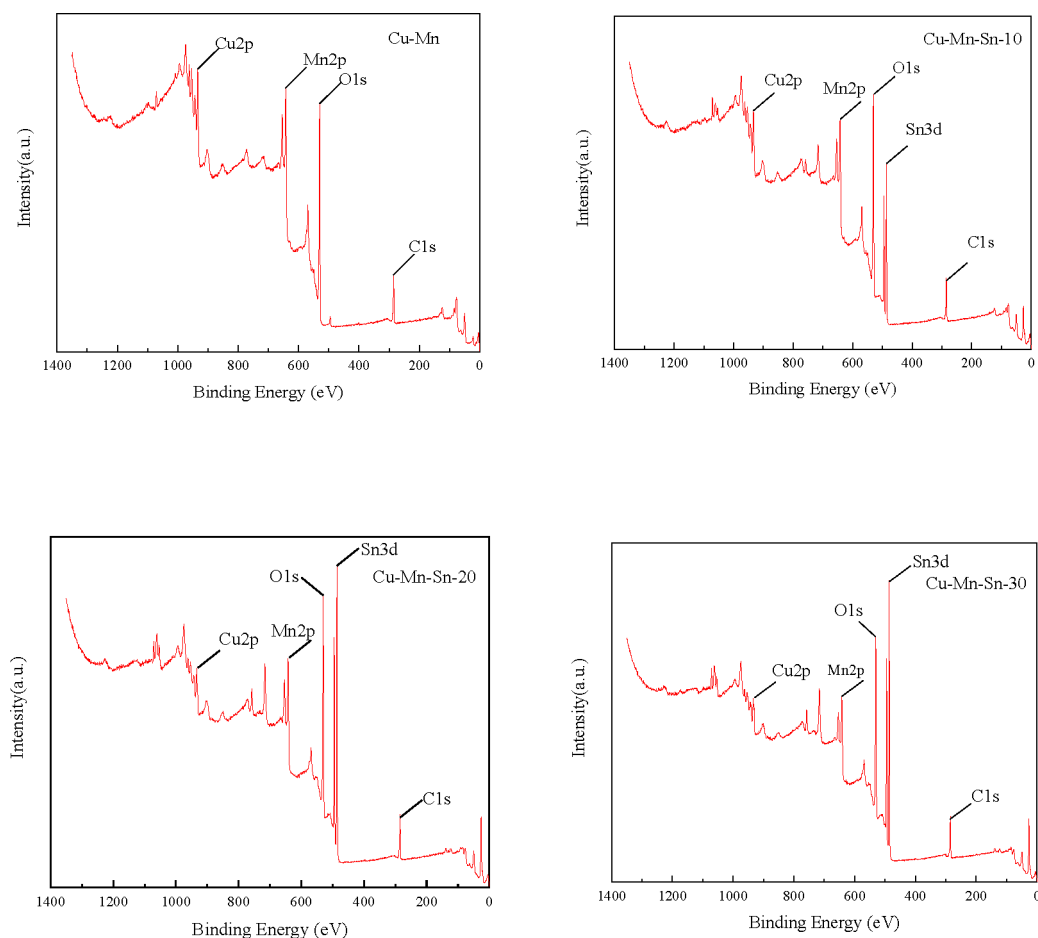
**Figure 11.** XPS scan full spectrum curve of elimination agent.

reacts with reactive oxygen species to form $CO_2$.[30] It can be seen that Sn doping improves the distribution of $Cu^{2+}$ on the surface of the eliminator, thus improving the activity of the eliminator.

**3.5. Water Resistance of Catalyst.** In order to study the effect of $H_2O$ on the elimination performance, Cu−Mn, hoplicate, and Cu−Mn−Sn-20 were prepared to absorb water for 10 h, and then the samples were scanned by FTIR to study the water absorption performance.

Sample preparation: 10 g of Cu−Mn, hoplicate, and Cu−Mn−Sn-20 was removed and put into the experimental system as shown in Figure 14. The humidity controller was used to control the humidity at the maximum of 95% in the mine. The sample was placed in a tray for 10 h, and the wet sample preparation was completed. Because of the great influence of free water on FTIR results, pure $N_2$ was used to purge the sample for 30 min to remove the physically adsorbed gas. Finally, the sample was taken out and put into the centrifugal tube for the experiment.

Figure 15 shows the FTIR spectrum of Cu−Mn, hoplicate, and Cu−Mn−Sn-20 samples after 10 h in a humid environment. According to Figure 15, Cu−Mn, hoplicate, and Cu−Mn−Sn-20 appear at an absorption peak at 3412 $cm^{-1}$ after completely absorbing water, which is hydroxyl (−OH) on the surface of the detergent.[25,31] However, an absorption peak appears at 1617 $cm^{-1}$. It indicates that $H_2O$ exists on the surface of the eliminator not in the form of hydroxyl (−OH) but in the form of lattice water. The peak with an absorption

spectrum of 3412 $cm^{-1}$ is the antisymmetric and symmetric OH stretching vibration, and the peak with an absorption spectrum of 1617 $cm^{-1}$ is the HOH bending vibration peak.

After the water was completely absorbed by Cu−Mn, hoplicate, and Cu−Mn−Sn-20, an absorption peak appeared at 1113 $cm^{-1}$, which was identified as the $[O_2^-]$ free radical. $[O_2^-]$ is obtained by the reaction of metal oxide with $O_2$ molecule in air, causing $O_2$ molecule to lose an electron. The higher the absorption peak of $[O_2^-]$ ions is, the higher the absorption peak of $[O_2^-]$ is, and the increase of $[O_2^-]$ indicates that the oxidability of eliminators is enhanced, and the adsorption of oxygen on the surface of eliminators is increased. This is the reason why the activity of Cu−Mn−Sn-10 is greater than that of Cu−Mn.

After the complete adsorption of water by Cu−Mn, hoplicate, and Cu−Mn−Sn-20, an absorption peak appears at 523 $cm^{-1}$, which is water in the coordination compound of $H_2O$ and Cu, and the spectral band is $\rho_w(H_2O)$. The results indicate that the lattice water and coordination water exist at the same time, and the absorption peak of coordination water is Cu−Mn > hoplicate > Cu−Mn−Sn-20. This rule showed an opposite pattern to the activity, indicating that coordination water had a greater influence on the activity of the eliminator, because the generation of coordination water occupied $Cu^{2+}$, and $Cu^{2+}$ provided the active site in the elimination process of the eliminator.[16,25]
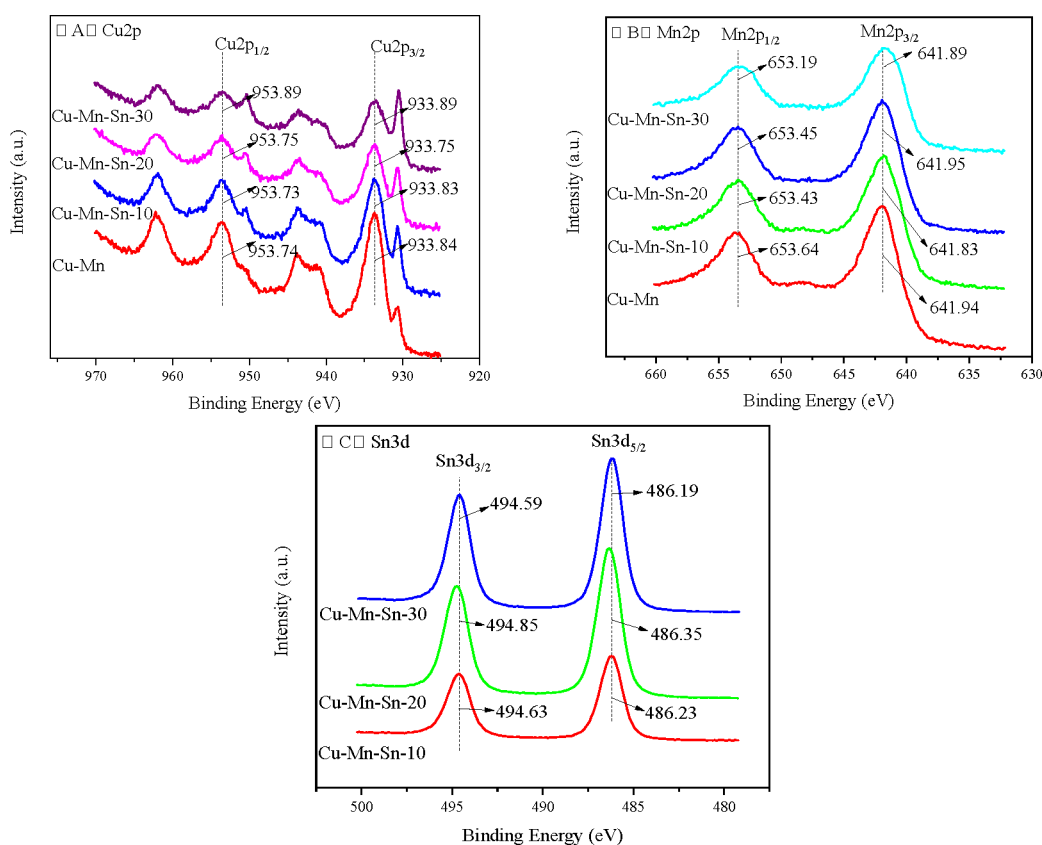
**Figure 12.** Elimination agent XPS scanning fine spectrum: (A) Cu 2p, (B) Mn 2p, (C) Sn 3d.
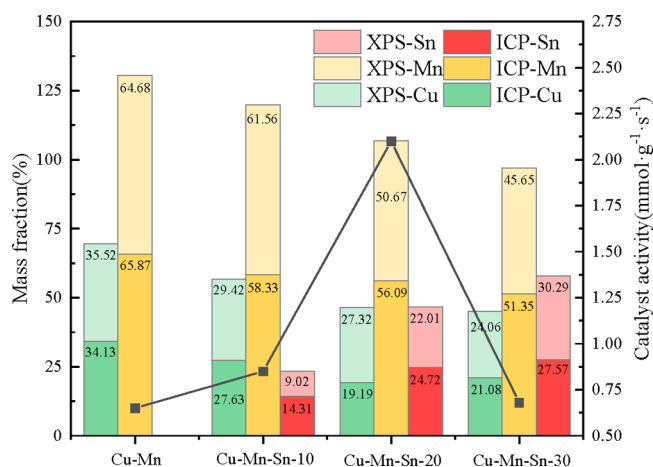


**Figure 13.** Relationship between surface element content and activity of remover.

## 4. CONCLUSIONS

In order to study the effect of Sn on the catalytic activity and water resistance of Cu−Mn catalyst CO, the elimination agent with Sn content of 0%, 10%, 20%, and 30% was prepared, where Cu/Mn = 1:2. The activity test and water resistance test of the sample were carried out, and the following conclusions were drawn:

(1) A test platform for the activity of eliminator was independently developed, the characterization indexes for the activity of eliminator were proposed, and activity tests on samples with different Sn contents were carried out. The results showed that the activity of Cu−Mn−Sn-20 eliminators showed an inverted U curve with Sn content, and the activity of Cu−Mn−Sn-20 eliminators with Sn content of 20% was the highest, which was 3.23 times that of Cu−Mn eliminators.

(2) $N_2$ adsorption and desorption were used to test the specific surface area and pore size of the samples with different Sn contents. The results showed that when all of the tested samples were mesoporous and the Sn content was 20%, the highest specific surface area was 86.04 $m^2 \cdot g^{-1}$ and the pore size was 10.88 nm, which improved the activity of the Cu−Mn−Sn type eliminators.

(3) A scanning electron microscope was used to observe the surface microstructure of samples with different Sn contents, and the sample morphologies were roughly the same, showing round particles. The Sn content has a significant effect on the surface morphology of the eliminator. With the doping of Sn, the particle size decreases obviously and the stack pore size becomes larger. Obviously, Cu−Mn−Sn-20 particles in Sn doped samples are more uniform in size, more regular in shape, and have abundant mesoporous structures, which provide larger specific surface area and more active sites and improve the activity of Cu−Mn−Sn type eliminators.

(4) X-ray diffraction and X-ray photoelectron spectroscopy were used to analyze the composition of the eliminators. For all eliminators, only $Cu_{1.4}Mn_{1.5}O_4$ and CuO phases were detected, and a large amount of MnOx and SnOx existed in the eliminators as amorphous phases. Sn and Cu exist in the eliminator in the state of complete oxidation of $Sn^{4+}$ and $Cu^{2+}$, while Mn has a mixed valence state, in which $Mn^{4+}$ dominates, and a small amount of $Mn^{2+}$ and $Mn^{3+}$ also exist in the eliminator. Cu−Mn−Sn-20 showed a CuO phase, and the crystallization degree of $Cu_{1.4}Mn_{1.5}O_4$ was lower, which improved the activity of the Cu−Mn−Sn type eliminators.
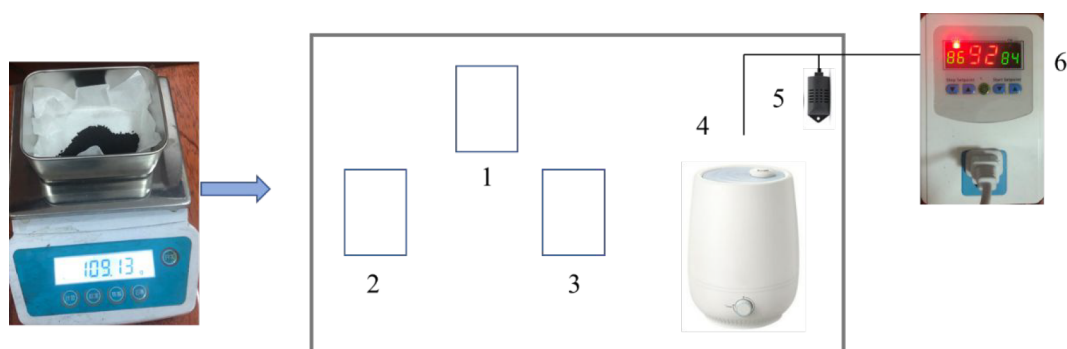
**Figure 14.** Experimental device: 1−3, trays for storing samples; 4, humidifier; 5, humidity sensor; 6, humidity controller.
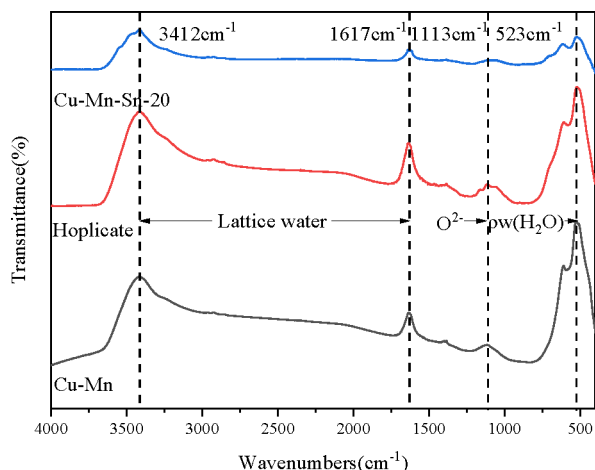


**Figure 15.** FTIR spectra of Cu−Mn, hoplicate, and Cu−Mn−Sn-20 after $H_2O$ is completely adsorbed.

(5) FTIR technology was used to study the adsorption behavior of the remover on $H_2O$. The adsorbed water on the surface of the remover has two states, namely lattice water and coordination water. The doping of Sn can inhibit the adsorption of water on the surface of the remover. The absorption of lattice water and coordination water is the least when the Sn content is 20%, which improves the water resistance of the Cu−Mn−Sn-type scavenger.

## AUTHOR INFORMATION

### Corresponding Author

**Yashengnan Sun** − *College of Safety Science and Engineering, Liaoning Technical University, Fuxin 123000, China; Key Laboratory of Mine Thermodynamic Disaster and Control of Ministry of Education, Huludao 125105, China;* orcid.org/0000-0003-4440-7294; Email: sunnn360@ 163.com

### Authors

**Xihua Zhou** − *College of Safety Science and Engineering, Liaoning Technical University, Fuxin 123000, China; Key Laboratory of Mine Thermodynamic Disaster and Control of Ministry of Education, Huludao 125105, China;* orcid.org/0000-0001-6235-6262

**Tianyu Xin** − *Institute of Mechanics and Engineering, Liaoning Technical University, Fuxin 123000, China;* orcid.org/ 0000-0002-2965-2921

**Gang Bai** − *College of Safety Science and Engineering, Liaoning Technical University, Fuxin 123000, China; Key Laboratory of Mine Thermodynamic Disaster and Control of Ministry of Education, Huludao 125105, China;* orcid.org/0000-0002-4599-6388

**Yumeng Wang** − *College of Safety Science and Engineering, Liaoning Technical University, Fuxin 123000, China; Key Laboratory of Mine Thermodynamic Disaster and Control of Ministry of Education, Huludao 125105, China*

**Xianlin Li** − *College of Safety Science and Engineering, Liaoning Technical University, Fuxin 123000, China; Key Laboratory of Mine Thermodynamic Disaster and Control of Ministry of Education, Huludao 125105, China*

**Xiao Mufeng** − *College of Architecture and Transportation, Liaoning Technical University, Fuxin 123000, China;* orcid.org/0000-0003-2529-1951

Complete contact information is available at:
https://pubs.acs.org/10.1021/acsomega.2c01002

## Notes

The authors declare no competing financial interest.

## REFERENCES

(1) Straub, F. Toxic Carbon Dioxide Exposures: The Unacceptable Risk. *Professional Safety* **2021**, *66* (07), 24−34.

(2) Sun, Y.; Zhou, X.; Bai, G.; Teng, Y.; Xin, T.; Xiao, M. Removal of CO Generated by a Gas Explosion Using a Cu-Mn Elimination Agent. *ACS Omega* **2021**, *6* (24), 16140−16150.

(3) Li, J.; Guo, Z.; Chen, X.; Zhou, F. Rapid and efficient removal of CO in CH4 and CH4/coal dust hybrid explosions: A novel approach of spraying catalyst powder. *Fuel* **2021**, *290*, 119790.

(4) Li, X.; Guo, R.; Qian, X. Preparation and absorption carbon monoxide properties of a novel flame retardants based fire-fighting foam. *Flame-Retardant Polymeric Materials and Polymer Composites* **2021**, DOI: 10.3389/fmats.2021.646509.

(5) Henn, S. A.; Butler, C.; Li, J.; Sussell, A.; Hale, C.; Broyles, G.; Reinhardt, T. Carbon monoxide exposures among U.S. wildland firefighters by work, fire, and environmental characteristics and conditions. *J. Occup Environ. Hyg* **2019**, *16* (12), 793−803.

(6) Hebda-Sobkowicz, J.; Gola, S.; Zimroz, R.; Wylomanska, A. Identification and Statistical Analysis of Impulse-Like Patterns of Carbon Monoxide Variation in Deep Underground Mines Associated with the Blasting Procedure. *Sensors (Basel)* **2019**, *19* (12), 2757.

(7) Huang, R.; Shen, X.; Wang, B.; Liao, X. Migration characteristics of CO under forced ventilation after excavation roadway blasting: A case study in a plateau mine. *Journal of Cleaner Production* **2020**, *267*, 122094.

(8) Hampson, N. B.; Bodwin, D. Toxic CO-ingestions in intentional carbon monoxide poisoning. *J. Emerg Med.* **2013**, *44* (3), 625−30.

(9) Poldorn, P.; Wongnongwa, Y.; Namuangruk, S.; Kungwan, N.; Golovko, V. B.; Inceesungvorn, B.; Jungsuttiwong, S. Theoretical mechanistic study of CO catalytic oxidation by O₂ on an ultra-small 13-atom bimetallic Ag₇Au₆ cluster. *Applied Catalysis A: General* **2020**, *595*, 117505.

(10) Jinzhang, J.; Fengxiao, W. Propagation of gas explosions in roadways with different cross-sectional shapes. *Energy Sources, Part A: Recovery, Utilization, and Environmental Effects* **2021**, *43*, 1−11.

(11) Yin, W.; Fu, G.; Yang, C.; Jiang, Z.; Zhu, K.; Gao, Y. Fatal gas explosion accidents on Chinese coal mines and the characteristics of unsafe behaviors: 2000−2014. *Safety Science* **2017**, *92*, 173−179.

(12) Zhou, G.; Zhang, L.; Liu, R.; Sun, B.; Kong, Y.; Huang, Z. Numerical simulation investigation for the pollution characteristics of dust particles in the fully mechanized mining face under different air humidity conditions. *Journal of Environmental Chemical Engineering* **2021**, *9* (6), 106861.

(13) Li, J.; Yang, L.; Song, T.; Qi, R. Research on the Effects of the High Temperature and Humidity Environment on Human Comfort in Coal Mine Emergency Refuge System. *Safety* **2019**, *5* (2), 28.

(14) Ma, D.; Qin, B.; Song, S.; Liang, H.; Gao, A. An Experimental Study on the Effects of Air Humidity on the Spontaneous Combustion Characteristics of Coal. *Combust. Sci. Technol.* **2017**, *189* (12), 2209−2219.

(15) Dey, S.; Dhal, G. C. Deactivation and regeneration of hopcalite catalyst for carbon monoxide oxidation: a review. *Materials Today Chemistry* **2019**, *14*, 100198.

(16) Liu, Y.; Guo, Y.; Peng, H.; Xu, X.; Wu, Y.; Peng, C.; Zhang, N.; Wang, X. Modifying Hopcalite catalyst by SnO₂ addition: An effective way to improve its moisture tolerance and activity for low temperature CO oxidation. *Applied Catalysis A: General* **2016**, *525*, 204−214.

(17) Bae, J.; Shin, D.; Jeong, H.; Kim, B.-S.; Han, J. W.; Lee, H. Highly Water-Resistant La-Doped Co₃O₄ Catalyst for CO Oxidation. *ACS Catal.* **2019**, *9* (11), 10093−10100.

(18) Yang, J.; Zhou, H.; Wang, L.; Zhang, Y.; Chen, C.; Hu, H.; Li, G.; Zhang, Y.; Ma, Y.; Zhang, J. Cobalt-Doped K-OMS-2 Nanofibers: A Novel and Efficient Water-Tolerant Catalyst for the Oxidation of Carbon Monoxide. *ChemCatChem.* **2017**, *9* (7), 1163−1167.

(19) Li, Q.; Zhou, X.; Zhao, W.; Peng, C.; Wu, H.; Chen, H. Pt/Fe co-loaded mesoporous zeolite beta for CO oxidation with high catalytic activity and water resistance. *RSC Adv.* **2019**, *9* (48), 28089−28094.

(20) Yin, C.; Liu, Y.; Xia, Q.; Kang, S.; Li, X.; Wang, Y.; Cui, L. Oxygen vacancy-rich nitrogen-doped Co₃O₄ nanosheets as an efficient water-resistant catalyst for low temperature CO oxidation. *J. Colloid Interface Sci.* **2019**, *553*, 427−435.

(21) Zhou, Y.; Yu, J.; Mao, D.; Mao, H.; Guo, X.; Sun, C.; Huang, H. A highly moisture-resistant binary M3Co16Ox composite oxide catalysts wrapped by polymer nanofilm for effective low temperature CO oxidation. *Applied Catalysis A: General* **2018**, *559*, 40−46.

(22) Shen, Y.; Yu, J.; Xiao, X.; Guo, X.; Mao, D.; Huang, H.; Lu, G. Polymer nanofilm-coated catalysis: An approach for enhancing water-resistance of Co-Fe oxide nano-catalysts under moisture-rich condition. *J. Catal.* **2017**, *352*, 466−479.

(23) Zhang, X.; Yang, Y.; Song, L.; Wang, Y.; He, C.; Wang, Z.; Cui, L. High and stable catalytic activity of Ag/Fe₂O₃ catalysts derived from MOFs for CO oxidation. *Molecular Catalysis* **2018**, *447*, 80−89.

(24) Li, Y.; Peng, H.; Xu, X.; Peng, Y.; Wang, X. Facile preparation of mesoporous Cu-Sn solid solutions as active catalysts for CO oxidation. *RSC Adv.* **2015**, *5* (33), 25755−25764.

(25) Xu, X.; Sun, X.; Han, H.; Peng, H.; Liu, W.; Peng, X.; Wang, X.; Yang, X. Improving water tolerance of Co₃O₄ by SnO₂ addition for CO oxidation. *Appl. Surf. Sci.* **2015**, *355*, 1254−1260.

(26) Zou, S.; Ji, Y.; Li, J.; Zhang, Y.; Jin, Z.; Jia, L.; Guo, X.; Zhong, Z.; Su, F. Novel leaflike Cu-O-Sn nanosheets as highly efficient catalysts for the Rochow reaction. *J. Catal.* **2016**, *337*, 1−13.

(27) Cai, L.-N.; Guo, Y.; Lu, A.-H.; Branton, P.; Li, W.-C. The choice of precipitant and precursor in the co-precipitation synthesis of copper manganese oxide for maximizing carbon monoxide oxidation. *J. Mol. Catal. A: Chem.* **2012**, *360*, 35−41.

(28) Mirzaei, A. A.; Shaterian, H. R.; Kaykhaii, M. The X-ray photoelectron spectroscopy of surface composition of aged mixed copper manganese oxide catalysts. *Appl. Surf. Sci.* **2005**, *239* (2), 246−254.

(29) Francisco, M. S. P.; Mastelaro, V. R.; Nascente, P. A. P.; Florentino, A. O. Activity and Characterization by XPS, HR-TEM, Raman Spectroscopy, and BET Surface Area of CuO/CeO₂-TiO₂ Catalysts. *journal of physical chemistry. B* **2001**, *105* (43), 10515−10522.

(30) Liu, Z.; Zhou, R.; Zheng, X. Preferential oxidation of CO in excess hydrogen over a nanostructured CuO-CeO₂ catalyst with high surface areas. *Catal. Commun.* **2008**, *9* (13), 2183−2186.

(31) Guo, Y.; Li, C.; Lu, S.; Zhao, C. Low temperature CO catalytic oxidation and kinetic performances of KOH-Hopcalite in the presence of CO₂. *RSC Adv.* **2016**, *6* (9), 7181−7188.